1 **hGRAD – a versatile 'one-fits-all' system for the acute depletion of RNA binding**

2 **proteins in nuclear condensates**

3

4 Benjamin Arnold[1,§], Ricarda J. Riegger[1,§], Ellen Kazumi Okuda[1], Irena Slišcović[1,2], Mario

5 Keller[1,2], François McNicoll[1], Kathi Zarnack[1,2] & Michaela Müller-McNicoll[1,#]

6

7 [1]Institute of Molecular Biosciences, Goethe University Frankfurt, Frankfurt am Main,

8 Germany

9 [2]Buchmann Institute for Molecular Life Sciences (BMLS), Goethe University Frankfurt,

10 Frankfurt am Main, Germany

11
12

13 [§]These authors contributed equally.

14 [#]Corresponding author:

15 email: mueller-mcnicoll@bio.uni-frankfurt.de

16
17

18 Keywords: hGRAD, RNA binding proteins, paraspeckles, nuclear speckles, rapid

19 degradation, GFP nanobody, SRSF5

20

21

22 Running title: hGRAD - versatile 'one-fits-all' rapid depletion

23

Abstract (159 words)

Nuclear RNA binding proteins (RBPs) are difficult to study because they often belong to large protein families and form extensive networks of auto- and cross-regulation. They are highly abundant and often localize to condensates with a slow turnover, requiring long depletion times or knockouts that cannot distinguish between direct and indirect or compensatory effects.

Here, we developed a system that is optimized for the rapid degradation of nuclear RBPs, called hGRAD. It comes as a 'one-fits-all' plasmid, and integration into any cell line that expresses endogenously GFP-tagged proteins allows an inducible, rapid and complete knockdown. We show that the nuclear RBPs SRSF3, SRSF5, SRRM2 and NONO are completely cleared from nuclear speckles and paraspeckles within two hours. hGRAD works in various cell types, is more efficient than other methods and does not require the expression of exogenous ubiquitin ligases. Combining SRSF5 hGRAD degradation with Nascent-seq uncovered highly dynamic transient transcript changes, compensatory mechanisms and that SRSF5 promotes transcript stability.

Introduction

RNA binding proteins (RBPs) often belong to larger protein families and form dense regulatory networks of auto- and cross-regulation, wherein they complement or antagonize each other's functions. These networks ensure the robustness of gene expression starting from transcription in the nucleus to translation and mRNA decay in the cytoplasm. This renders it very challenging to disentangle the specific functions of individual RBPs and their relationship to human diseases (Gebauer et al., 2021; Müller-McNicoll et al., 2019). Most RBPs are also highly abundant and stable proteins, and many of them localize to nuclear condensates with a slow turnover, which makes it difficult to deplete them using RNA interference. On the other hand, complete knockouts (KOs) or very long depletion times trigger compensatory effects and do not allow to distinguish between direct and indirect effects.

One example for such a large family of nuclear RBPs are the serine/arginine-rich splicing factors (SRSF1-SRSF12, SR proteins) that are present in all metazoans (Sliskovic et al., 2022). SR proteins are essential factors for constitutive and alternative pre-mRNA splicing (AS), and they also influence many other steps in mRNA metabolism including transcription, alternative polyadenylation, mRNA packaging, export, translation and cytoplasmic decay (Jeong, 2017; Wegener and Müller-McNicoll, 2019; Änkö, 2014). SR proteins also participate in the processing of non-coding RNAs and the formation and dynamics of nuclear compartments (de Oliveira Freitas Machado et al., 2023; Königs et al., 2020; Wagner and Frye, 2021). In contrast to their canonical functions in splicing, the participation of individual SR protein family members in specific AS events or other disease-related, non-canonical functions remains poorly understood. This is in part because SR- and SR-like proteins cooperate and compete for binding sites, compensate for each other, and the removal of one SR protein can affect the levels of several other family members (Meinke et al., 2020; Änkö et al., 2012). Dysregulated levels of individual SR protein family members are associated with various cancers and other diseases including neurological disorders, liver disease as well as coronary and cardiac diseases (More and Kumar, 2020; Ratnadiwakara et al., 2018; Zheng et al., 2020). Because

70   of their overlapping functions and compensatory mechanisms, specific inducible protein

71   degradation systems with short depletion times are needed to disentangle the functions

72   of individual SR proteins and other RBPs.

73   Proteins are usually targeted for degradation by the addition of polyubiquitin

74   chains to lysine residues which are recognized by the 26S proteasome (Komander and

75   Rape, 2012; Yu and Matouschek, 2017). In a highly regulated multi-enzymatic reaction,

76   ubiquitin (Ub) is first activated by E1 enzymes under ATP consumption, subsequently

77   transferred to E2-Ub-conjugation enzymes and finally transferred to target proteins by

78   E3-Ub-ligases. More than 600 different E3-Ub-ligases are encoded in the human genome,

79   enabling target specificity (Nakayama and Nakayama, 2006). The RING-finger family

80   contains the SKP1-Cullin-F-box protein (SCF) complex, which is the most prominent E3-

81   Ub-ligase in mammals (Frescas and Pagano, 2008; Schulman et al., 2000). Its subunit

82   RBX1 facilitates E2-Ub recruitment and the ubiquitylation reaction, CUL1 functions as a

83   bridge and SKP1 mediates binding to a modular F-box protein (FBP). More than 70

84   different FBPs are encoded in the human genome, providing additional target specificity

85   (Frescas and Pagano, 2008; Schulman et al., 2000). FBPs have two major domains: the F-

86   box domain, which is essential for the interaction with SKP1, and a variable C-terminal

87   domain, which is essential for target recognition (Kipreos and Pagano, 2000).

88   Most targeted protein degradation approaches manipulate the SCF complex by

89   introducing an engineered FBP with specificity for a protein-of-interest (POI). Examples

90   are the deGradFP system (Caussinus et al., 2011) and the auxin-inducible degron (AID)

91   systems (Li et al., 2019; Nishimura et al., 2009). The deGradFP system was developed to

92   degrade GFP-tagged proteins in *Drosophila melanogaster.* Here, the substrate recognition

93   of the F-box protein Slmb was altered by fusing its minimal F-box to a synthetic anti-

94   GFP nanobody (VHH-GFP4) (Rothbauer et al., 2008) replacing the C-terminal WD40

95   repeat domain (Caussinus et al., 2011). Nanobodies are small proteins (10-15 kDa) that

96   resemble the variable fragment (VHH) of homodimeric heavy chain antibodies, derived

97   from camelids (Harmsen and De Haard, 2007). They are highly stable, can be easily

4

98　expressed in mammalian cells and bind strongly to their specific antigens (Beghein and

99　Gettemans, 2017). Upon inducible expression of the F-box-nanobody fusion protein, the

100　GFP-tagged POI is bound, endogenous SKP1, CUL1 and RBX1 are recruited, and

101　ubiquitylation and degradation are initiated. The deGradFP system degrades GFP-

102　tagged proteins in *Drosophila* with a half-life of 2 hours and is also functional for several

103　GFP derivates like Venus, YFP and EYFP (Caussinus and Affolter, 2016; Caussinus et al.,

104　2011). It was successfully adapted to other model organisms, such as *Danio rerio* and

105　*Trypanosoma brucei* (Ishii and Akiyoshi, 2022; Yamaguchi et al., 2019), but so far failed to

106　degrade nuclear proteins in mammalian cells (Daniel et al., 2018; Ludwicki et al., 2019;

107　Shin et al., 2015).

108　　　　In the AID systems, the plant hormone auxin (indole-3-acetic acid, IAA or AUX)

109　induces target protein degradation via the SCFs osTIR1 from *Oriza sativa* (Nishimura et

110　al., 2009) or aaAFB2 from *Arabidopsis thaliana* (Li et al., 2019). Upon AUX binding, osTIR1

111　undergoes a structural change allowing stable interactions with AID sequences in target

112　proteins, which are subsequently ubiquitylated and degraded (Holland et al., 2012;

113　Nishimura et al., 2009; Trost et al., 2016). AID sequences can be fused directly to the

114　target proteins or to nanobodies, which can be inducibly expressed and bind to the

115　target protein. Upon addition of AUX, degradation occurs within 20-60 minutes, and is

116　stopped upon AUX withdrawal (Daniel et al., 2018; Holland et al., 2012; Li et al., 2019;

117　Nishimura et al., 2009). Despite these advantages, AID systems require the constitutive

118　expression of large foreign FBPs, which is often toxic for cells, and they are leaky

119　showing basal degradation without auxin induction.

120　　　　An alternative degradation system that functions independently of the SCF

121　complex is called Trim-Away and is based on the E3-Ub-ligase tripartite motif-

122　containing protein 21 (TRIM21), which confers target specificity and E3-Ub-ligase

123　activity (Clift et al., 2017). TRIM21 recognizes and binds the Fc region of antigen-bound

124　antibodies (IgG) and mediates their ubiquitylation and degradation (James et al., 2007).

125　This system enables a rapid and efficient degradation of cytoplasmic proteins, with half-

126   lives of 10-30 minutes. However, target-specific antibodies need to be delivered into cells

127   by electroporation which, due to their large size, cannot diffuse through the nuclear pore

128   and thus cannot be used to deplete nuclear proteins (Clift et al., 2017).

129   Here, we present hGRAD, short for human protein degradation system, which is

130   optimized to induce the rapid and efficient degradation of GFP-tagged nuclear RBPs

131   from various subnuclear compartments. hGRAD allowed us to identify a novel function

132   of SRSF5 in promoting transcript stability and to define direct target genes and

133   compensatory mechanisms.

134

Results

Development of the hGRAD system

To study the functions of nuclear RBPs, we aimed to develop a rapid degradation system that is easy to implement, requires minimal engineering of host cells and efficiently degrades RBPs that localize to nuclear condensates. Ideally, it should function in different species, cell types and subcellular compartments, and allow to follow the kinetics of degradation in real time. We decided to target GFP-tagged proteins, since many groups use endogenous GFP tagging by CRISPR/Cas9 to study the functions of condensate RBPs and many tagged cell lines are commercially available.

We first designed a 'one-fits-all' plasmid expression system, which allows the inducible expression of two genes in a doxycycline (DOX)-dependent manner (**Figure 1A**). This vector, named pTRE-BI, expresses a Tet-regulator (Tet-on 3G) from the *EF-1α* promoter which drives robust constitutive expression independently of mammalian cell type and species. It also contains a bi-directional tet-inducible promoter (TRE3G BI) with two flanking multiple cloning sites (MCS) and a puromycin resistance gene (PuroR) for genomic integration and selection (**Figure 1A**).

Next, we modified the deGradFP system (Caussinus et al., 2011), since previous studies indicated that deGradFP is inefficient in degrading nuclear proteins in mammalian cells (Daniel et al., 2018). In humans, more than 70 different FBPs have been reported that mediate target selection and specificity (Frescas and Pagano, 2008; Jin et al., 2004; Zheng et al., 2002). We identified the human protein FBXW11 as the closest ortholog to *Drosophila* Slmb (**Figure 1B**) and fused its minimal F-box domain to an anti-GFP nanobody (VHH-GFP4). The F-box-nanobody fusion was inserted on one side of the bi-directional TREG3 BI promoter and mCherry as induction control on the other side. The Tet-regulator activates the transcription of both genes upon DOX addition. We named our 'one-fits-all' plasmid system hGRAD for human protein degradation system (**Figure 1C**). Random genomic integration of this vector should allow the inducible degradation of any GFP-tagged protein through binding of the anti-GFP nanobody and

7

163 recruitment of the cellular SCF complex, which mediates ubiquitylation and

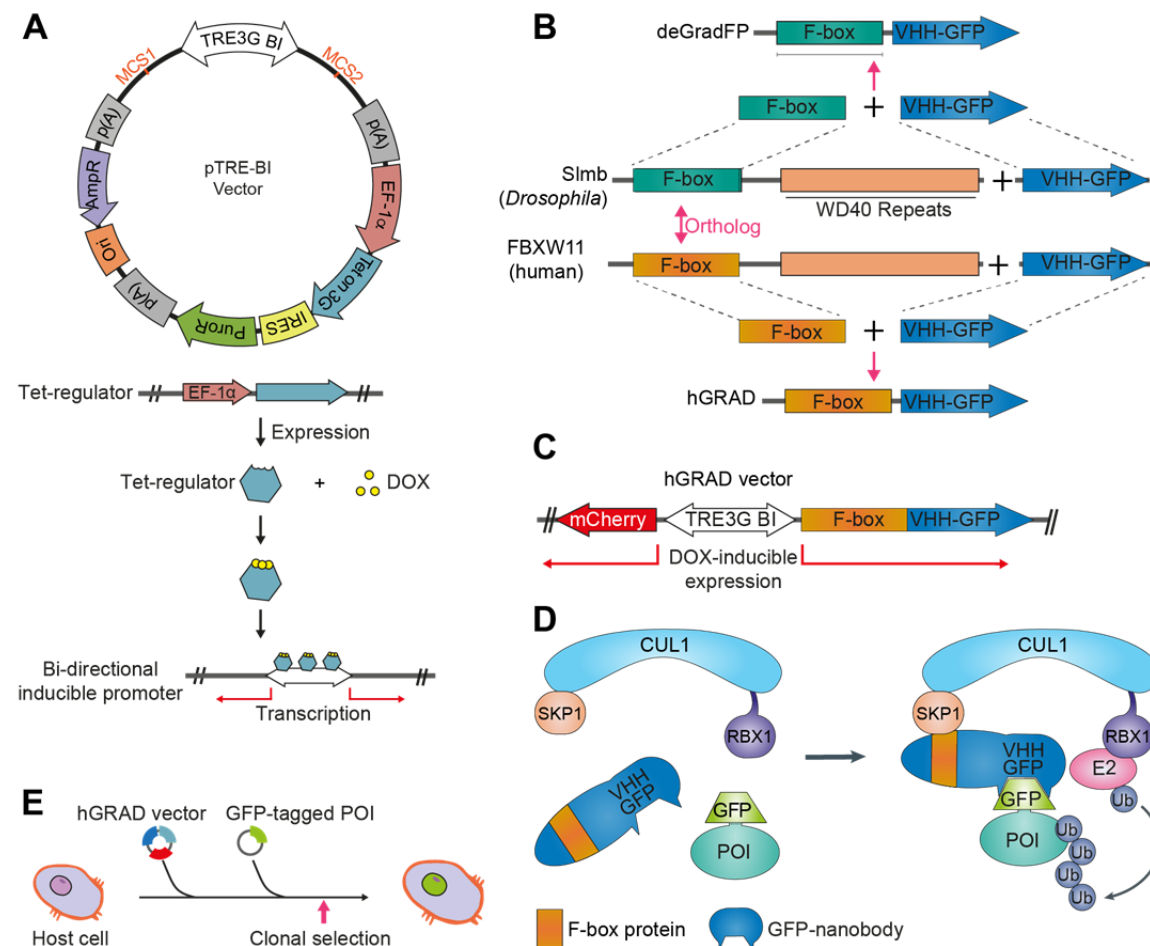164 proteasomal degradation (**Figure 1D, 1E**).

165

Figure 1. Development of the hGRAD system. A) Scheme of the pTRE-BI 'one-fits-all' backbone vector. MCS1 and MCS2, multiple cloning sites; p(A), polyadenylation sites; *EF-1α*, promoter; Tet on 3G, gene encoding Tet-regulator; IRES, internal ribosomal entry site; PuroR, puromycin resistance gene; Ori, origin of replication; AmpR, ampicillin resistance gene. **B)** The hGRAD system is based on the deGradFP system (Caussinus et al., 2011) and was optimized for mammalian protein degradation by exchanging the *Drosophila* Slmb F-box domain with the human FBXW11 F-box domain. **C)** Scheme of the pTRE-BI hGRAD vector. **D)** Overview of the hGRAD system harnessing the cellular SCF complex for ubiquitylation and degradation of the GFP-tagged protein-of-interest (POI). Model modified from (Yamaguchi et al., 2019). **E)** Random genomic integration of the pTRE-BI-hGRAD plasmid allows the inducible degradation of any GFP-tagged protein in any mammalian host cell type.

176

hGRAD degrades nuclear RBPs more efficiently than other degradation systems

178 To be able to compare the performance of hGRAD in degrading mammalian

179 GFP-tagged proteins with other rapid degradation systems, we modified the target

180 specificity of osTIR1, aaAFB2 (AID systems) and TRIM21 (Trim-Away system) through

181   anti-GFP nanobodies and cloned all necessary protein-coding sequences in the pTRE-BI

182   vector (**Figure 2A**): genes encoding *osTIR1* and *aaAFB2* were fused to mCherry and to a

183   weak nuclear localization sequence (NLS) at their C-terminus to ensure optimal

184   degradation of cytoplasmic and nuclear proteins. The gene fusions were then inserted

185   on one side of the bidirectional promoter. On the other side, a sequence encoding a GFP

186   nanobody fused to the minimized AID (mAID) sequence was inserted for the osTIR1

187   system (Daniel et al., 2018), while for the aaAFB2 system, an optimized AID sequence

188   (miniIAA7) was used (Li et al., 2019). For the Trim-Away system, the *TRIM21* gene was

189   also fused to mCherry and a weak NLS, and the anti-GFP nanobody was fused to the Fc

190   region of human IgG1 (Clift et al., 2017) (hIgG1-Fc2; **Figure 2A**).

191   We generated four master cell lines by integrating the different pTRE-BI

192   constructs into the genome of wild-type (WT) HeLa cells and selecting single clones. All

193   pTRE-BI-based induction systems showed a strong DOX-induced expression of the

194   desired proteins and no expression in the uninduced state (**Figure 2B**). Despite their

195   large molecular weights (>100 kDa), all mCherry fusion proteins localized to both the

196   cytoplasm and the nucleus (**Figure S1A**), demonstrating that the weak NLS is functional.

197   Thus, targeted protein degradation should occur in both subcellular compartments

198   (Franic et al., 2021).

199   We next performed proliferation assays to evaluate potential adverse effects of

200   the DOX treatment. The four master cell lines were grown in the presence or absence of

201   DOX (1 μg/mL; 72 h) and doubling times (t_d) were calculated. The osTIR1, aaAFB2,

202   TRIM21 and hGRAD cell lines showed similar growth rates compared to WT HeLa cells

203   in the absence of DOX (t_d=17.23 h), suggesting that the integrated pTRE-BI plasmid itself

204   does not negatively affect cell growth (**Figure S1B**). However, upon DOX addition, the

205   osTIR1 (t_d=19.3 h), aaAFB2 (t_d=20.84 h) and TRIM21 (t_d=18.41 h) cell lines showed

206   reduced growth rates, indicating potential cytotoxic effects from the enzymatic activity

207   or expression of the heterologous proteins. In contrast, the hGRAD cells showed similar

208   doubling times (t_d=17.24 h) to WT cells, indicating that expression of the hGRAD

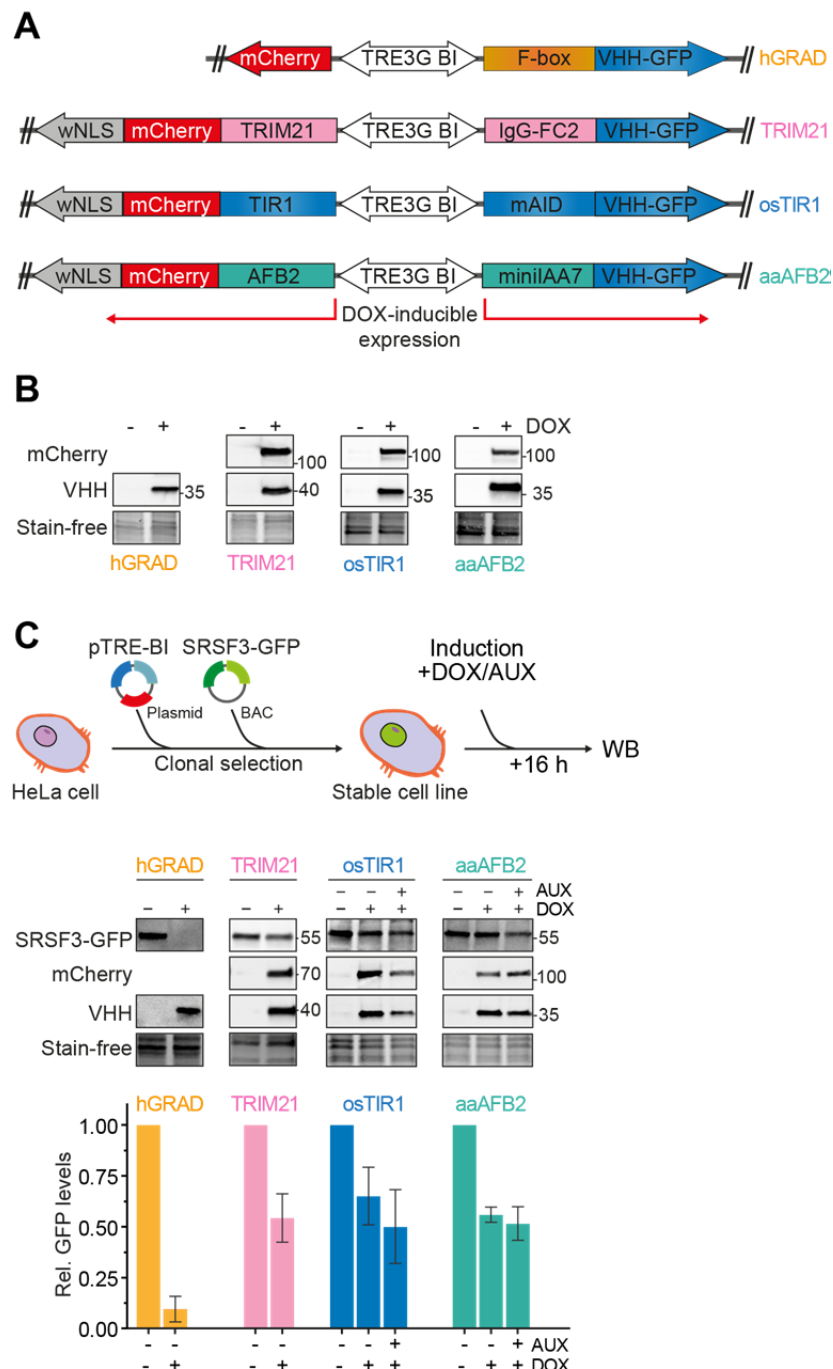209   components does not affect cell growth (**Figure S1B**).

9

Figure 2. hGRAD degrades the nuclear RBP SRSF3 more efficiently than other degradation systems in HeLa cells. A) Schemes of the pTRE-BI 'one-fits-all' vectors for expression of the TRIM21, hGRAD, osTIR1 and aaAFB2 systems. **B)** Induction in HeLa cells (16 h, 1 µg/mL DOX, 0.5 mM AUX). TRIM21-, osTIR1- and aaAFB2-mCherry fusion proteins were detected by an anti-mCherry antibody. The different nanobody fusions (IgG-Fc2-, FBXW11-, mAID- and miniIAA7-VHH-GFP) were detected by an anti-camelid VHH antibody. Stain-free gels were used to detect total protein and control for equal loading. **C)** Experimental scheme and comparison of the degradation efficiencies of TRIM21, hGRAD, osTIR1 or aaAFB2 systems after 16 h DOX and AUX induction. SRSF3-GFP, mCherry and the hGRAD nanobody fusion were detected with anti-GFP, anti-mCherry and anti-camelid antibodies, respectively. Shown are a representative Western blot and the quantification of n=3 independent replicates. Error bars show standard deviation of the mean (SD).

10

221   To compare the efficiency in targeting and degrading GFP-tagged SR proteins,

222   we inserted a bacterial artificial chromosome (BAC) harboring the *SRSF3* gene fused to a

223   GFP-tag into the genome of all four master cell lines (**Figure S1C**). The BAC gene

224   harbors the complete *SRSF3* gene, including the endogenous *SRSF3* promoter,

225   untranslated regions (UTRs), exons and introns so that *SRSF3-GFP* is expressed,

226   processed and regulated similarly to the endogenous gene (Müller-McNicoll et al., 2016).

227   All four cell lines showed similar SRSF3-GFP levels and the expected localization to the

228   nucleoplasm and nuclear speckles (**Figure S1D**).

229   After DOX treatment (16 h), all proteins required for rapid degradation were

230   strongly expressed (**Figure 2C**). The hGRAD system showed an almost complete

231   degradation of SRSF3-GFP (**Figure 2C**). In contrast, the TRIM21, osTIR1 and aaAFB2

232   systems reduced SRSF3-GFP levels by only about 50% in the presence of AUX (16 h).

233   Moreover, in the osTIR1 and aaAFB2 systems, SRSF3-GFP levels were already reduced

234   in the presence of DOX without AUX, indicating that the AID system is leaky, in line

235   with previous findings (Verma et al., 2020).

236   Our data demonstrate that the 'one-fits-all' pTRE-BI vector backbone allows a

237   strong and tightly controlled inducible expression of the factors required for

238   degradation of both nuclear and cytoplasmic proteins. Compared to the osTIR1, aaAFB2

239   and TRIM21 systems, hGRAD showed the most efficient depletion of a nuclear RBP and

240   mildest cytotoxic effects.

241

242   **hGRAD efficiently degrades RBPs that localize to nuclear condensates**

243   We next evaluated the capacity of hGRAD to degrade GFP-tagged proteins in

244   different subcellular compartments. For this, we stably integrated BACs expressing

245   eukaryotic translation initiation factor 4E (EIF4E-GFP) and serine/arginine-rich protein-

246   specific kinase 1 (SRPK1-GFP) as cytoplasmic marker proteins, SRSF5-GFP as marker for

247   nuclear speckles and Non-POU domain-containing octamer-binding protein (NONO-

248   GFP) as a marker for paraspeckles into the HeLa hGRAD cell line (**Figure 3A**). The

249   correct subcellular localization of the GFP-tagged proteins was confirmed by confocal

250   microscopy (**Figures 3D, S2A**). Western blot experiments revealed that the hGRAD-

251   mediated degradation worked most efficiently for proteins localizing to nuclear speckles

252   (SRSF3 and SRSF5) or paraspeckles (NONO; > 90%), while cytoplasmic proteins were

253   degraded slightly less efficiently (EIF4E and SRPK1; **Figure 3B**). This was confirmed by

254   confocal microscopy (**Figure S2A**).

255   To separate direct from indirect effects, a fast depletion of a protein is most

256   desirable. To evaluate the kinetics of hGRAD-mediated degradation, we performed a

257   time-course for SRSF3, SRSF5, NONO and EIF4E (0, 2, 4, 6 and 8 h DOX; **Figure 3C**).

258   Proteins were already reduced after 2 h post-induction, concomitant with expression of

259   the anti-GFP nanobody. The depletion efficiency differed among the GFP-tagged

260   proteins. Nuclear SRSF3-, SRSF5- and NONO-GFP were degraded rapidly, with half-

261   lives of 2.0 h and 2.5 h and almost 90% depletion after 6 and 8 h respectively.

262   Cytoplasmic EIF4E-GFP was degraded slightly slower, with a half-life of 3.3 h and 75%

263   depletion after 8 h (**Figure 3C**, **S2B**).

264   To monitor degradation in individual cells over time, we combined rapid

265   degradation with confocal live-cell imaging. HeLa hGRAD cell lines expressing SRSF3-

266   GFP or SRSF5-GFP were imaged in the presence or absence of DOX for 12 hours.

267   Relative GFP intensity was quantified in individual cells and normalized to the first

268   uninduced time point (t0). Similar to the Western blot quantifications, SRSF3-GFP

269   revealed a half-life of 2.2 h and SRSF5-GFP of 2.5 h (**Figure 3D**). Both proteins reached

270   their minimum levels (below 10% compared to t0) after 4 and 4.5 h of induction,

271   respectively. This indicates that hGRAD degradation of nuclear proteins in individual

272   cells has similar kinetics to bulk cell measurements. Thus, hGRAD quickly and

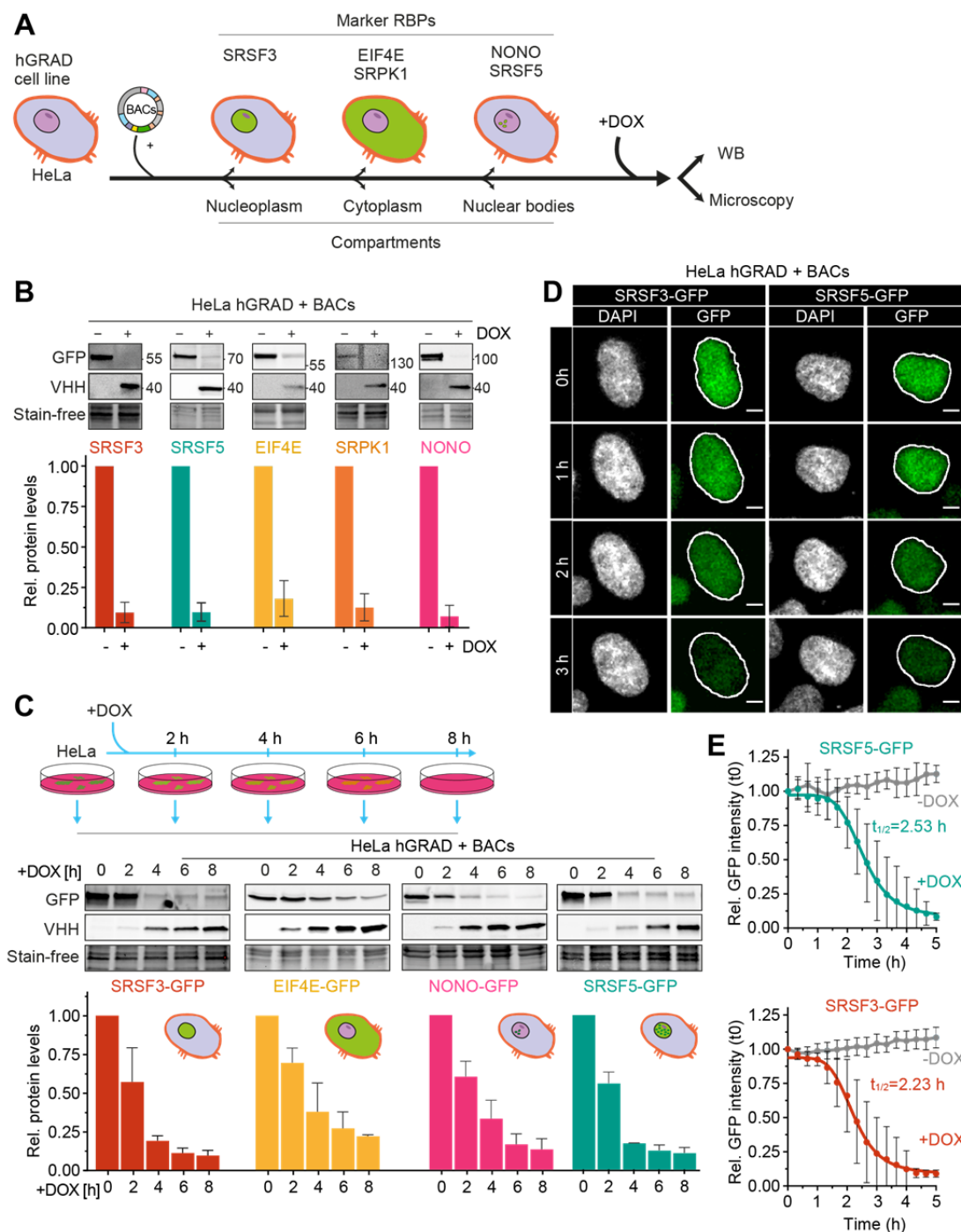273   efficiently clears proteins from nuclear condensates within three hours.

274

Figure 3. hGRAD works efficiently for RBPs that localize to nuclear condensates. A) Experimental scheme to test the hGRAD degradation for human proteins localizing to different subcellular compartments. **B)** Comparison of the degradation efficiency of GFP-tagged RBPs in HeLa cells 16 h after DOX induction (1 μg/mL). **C)** Degradation time-courses show that hGRAD works most efficiently for nuclear RBPs. **B+C)** Shown are the quantifications of n=3 independent Western blot experiments and one representative blot relative to the -DOX or 0 h time point. GFP-tagged proteins and the hGRAD nanobody fusion were detected with anti-GFP and anti-camelid antibody, respectively. **D)** Live-cell imaging to follow the hGRAD degradation kinetics. **E)** Quantification of half-lives ($t_{1/2}$) of SRSF3- and SRSF5-GFP in HeLa cells upon DOX induction. Scale bars = 5 μm. Error bars, SD.

13

285 **hGRAD works efficiently in different mammalian cell types and species**

286   We next evaluated the capacity of hGRAD to degrade GFP-tagged proteins in

287 pluripotent mouse P19 cells. For this, we generated a P19 hGRAD master cell line and

288 integrated BACs expressing SRSF3-, EIF4E-, SRPK1- and NONO-GFP into the genome

289 (**Figure S2B**). Similar to HeLa cells, the anti-GFP nanobody fusion was well expressed

290 upon DOX induction (1 μg/mL)nand undetectable in the absence of DOX in P19 cells,

291 indicating a strong inducibility and no leaky expression (**Figure 4A**). Proliferation assays

292 revealed that neither integration of the pTRE-BI-hGRAD vector itself (uninduced) nor

293 DOX induction showed any significant changes in growth rates compared to WT P19

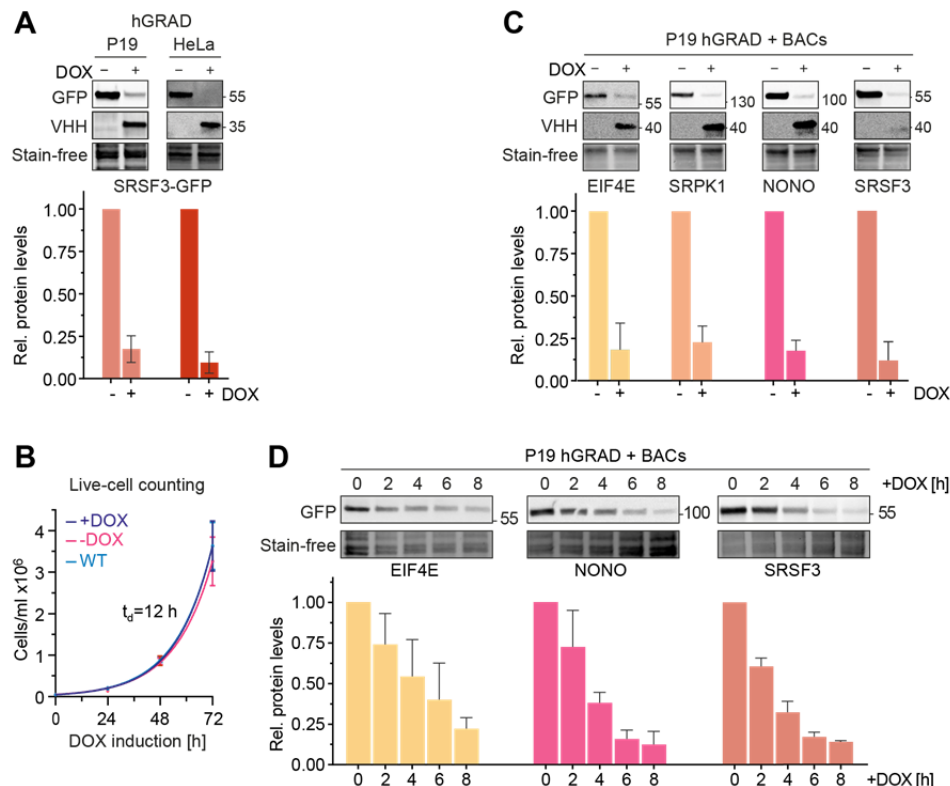294 cells with the characteristic doubling time of 12 h (**Figure 2B**).

295
296 **Figure 4. hGRAD works efficiently in different mammalian cell types and species. A)** Comparison of the
297 degradation efficiency of GFP-tagged SRSF3 in HeLa and P19 cells 16 h after induction with DOX (1 μg/mL).
298 **B)** P19 hGRAD proliferation assay. Growth curves and doubling times (t_d) were evaluated by exponential
299 growth equation fit ($Y=Y_0*exp(k*X)$). P19 WT (light blue), P19 hGRAD -DOX (pink), P19 hGRAD +DOX
300 (dark blue). Shown are mean and SD (error bars) from n=3 independent experiments. **C)** Comparison of the
301 degradation efficiency of GFP-tagged proteins in mouse P19 cells 16 h after DOX induction. **D)** Degradation
302 time-courses show that hGRAD works efficiently in mouse P19 cells. **A-D)** Shown are one representative
303 Western blot and the quantifications of n=3 independent experiments (relative to the -DOX or 0 h time
304 point). GFP-tagged proteins and the hGRAD nanobody fusion were detected with anti-GFP and anti-
305 camelid antibody, respectively. Error bars = SD.

14

306
307   Endpoint degradation assays and GFP fluorescence microscopy confirmed the efficient

308   depletion of all tested proteins in P19 cells (**Figure 4C, S2A**). SRSF3- and NONO-GFP

309   showed a half-life of 2.9 h post-induction and EIF4E-GFP of 4.3 h (**Figure 4D, S2B**).

310   Thus, our data demonstrate that the hGRAD system allows efficient degradation of GFP-

311   tagged proteins in both human HeLa and mouse P19 cells.

312

313   **hGRAD works as a rapid knockdown tool for endogenously GFP-tagged nuclear**

314   **RBPs**

315   We next tested the capacity of hGRAD in degrading endogenously GFP-tagged

316   proteins (endo-GFP) as a rapid knockdown tool. For this, we inserted a GFP-tag at the C-

317   termini of *SRSF3*, *SRSF5* and the nuclear speckle marker *SRRM2* in HeLa and P19

318   hGRAD master cell lines using CRISPR/Cas9 (**Figure 5A**). Successful GFP-tagging of

319   single clones was validated by PCR, Sanger sequencing and Western blot (**Figure S3A-**

320   **D**). Confocal microscopy revealed the correct nuclear localization of SRSF3-endo-GFP

321   and SRSF5-endo-GFP, with their typical distribution in the nucleoplasm and enrichment

322   within nuclear speckles, as well as of SRRM2-endo-GFP, which exclusively localized to

323   nuclear speckles (**Figure S3E**). We concluded that all endogenously tagged proteins

324   were correctly folded and fully functional.

325   Endpoint degradation assays revealed that SRSF3-endo-GFP and SRSF5-endo-

326   GFP were efficiently depleted in HeLa cells (by more than 90%; **Figure 5B**), similar to the

327   system where they were expressed from BACs (see above). Time-course experiments

328   indicated a half-life of 2.2 h for SRSF3-endo-GFP (**Figure 5C**), reaching its minimum

329   after 4 h, similar to SRSF3-GFP from the BAC (2.0 h, **Figure 3C**). SRRM2-endo-GFP

330   showed a half-life of 2.2 h and reached its minimum after 6 h, demonstrating that

331   hGRAD is capable of degrading nuclear proteins that make the core of nuclear speckles

332   (**Figure 5D**). SRSF5-endo-GFP showed a half-life of 2.1 h after DOX induction and

333   reached its minimum levels after 4 h (**Figure 5C**). For comparison, the BAC-expressed

15

334   SRSF5-GFP showed a half-life of 2.5 h, suggesting that SRSF5-endo-GFP is degraded

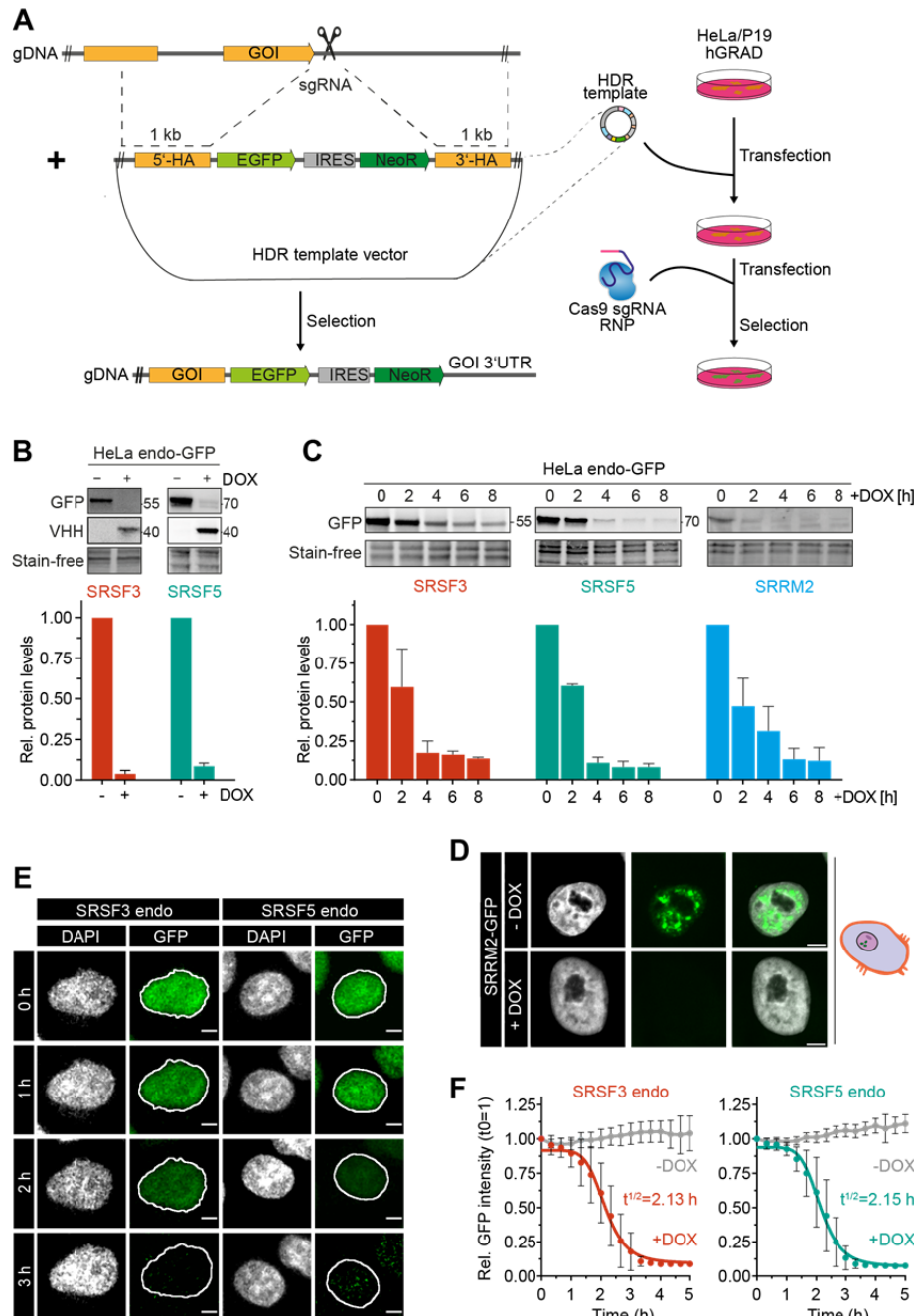335   slightly faster (**Figure 3C, 5C**).

336
337

338
339   **Figure 5. hGRAD efficiently degrades endogenously GFP-tagged nuclear RBPs in HeLa cells allowing**
340   **their rapid knockdown. A)** Experimental scheme for the endogenous (endo) GFP-tagging using
341   CRISPR/Cas9 in HeLa and P19 hGRAD cells. gDNA - genomic DNA; sgRNA - single guide RNA; GOI -
342   gene of interest; HDR - homology-directed repair; NeoR - Neomycin resistance cassette; 5' and 3'HA -

343 homology arms. **B)** Comparison of the degradation efficiency of SRSF3- and SRSF5-endo-GFP in HeLa cells
344 16 h after induction by DOX. **C)** Degradation time-courses show that hGRAD works efficiently for SRSF3-,
345 SRSF5- and SRRM2-endo-GFP. **B+C)** Shown are a representative Western blot and the quantification of n=3
346 independent experiments. Error bars = SD. GFP-tagged proteins and hGRAD nanobody fusion proteins
347 were detected with anti-GFP and anti-camelid antibody, respectively. **D)** Degradation of SRRM2-GFP from
348 nuclear speckles. Scale bars = 5 μm. **E)** Live-cell imaging reveal hGRAD degradation kinetics. **F)**
349 Quantification of the half-lives ($t_{1/2}$) of SRSF3- and SRSF5-endo-GFP in HeLa cells.
350

351 Degradation of SRSF5-endo-GFP was blocked when cells were treated with the

352 proteasome inhibitor MG132 (**Figure S3F**), confirming that degradation occurs via the

353 ubiquitin-proteasome system. In P19 cells, degradation kinetics of SRSF3-endo-GFP and

354 SRSF5-endo-GFP were similar to those in HeLa cells (**Figure S4A, S4B**); both proteins

355 were depleted by 80-90% after 6 h. Live-cell imaging confirmed that SRSF3- and SRSF5-

356 endo-GFP were depleted slightly faster than their counterparts expressed from BACs,

357 with half-lives of 2.13 h and 2.15 h, respectively (**Figure 5E, 5F**).

358 Interestingly, hGRAD depletion of SRSF5-endo-GFP worked with similar

359 efficiency independently of the glucose concentration (**Figure S4D**), although a previous

360 study proposed that SRSF5 is much less stable under low glucose conditions (Chen et al.,

361 2018). We also did not observe any differences in SRSF5-endo-GFP protein half-lives in

362 high and low glucose conditions (**Figure S4C**). Altogether, our data show that hGRAD

363 efficiently degrades endogenously GFP-tagged SRSF3, SRSF5 and SRRM2, the former in

364 HeLa and P19 cells. This underlines that the simple one-step integration of the hGRAD

365 plasmid into any cell line that expresses endogenously GFP-tagged proteins allows their

366 rapid and inducible knockdown.

367

368 **Combining hGRAD with Nascent-seq reveals dynamic changes in transcript levels**

369 Conventional knockdown of SRSF5 using siRNAs required 72 h to obtain a 75%

370 reduction at the protein level (**Figure S5A**). These long depletion times render it difficult

371 to distinguish direct from indirect targets or identify new functions of SRSF5 due to

372 compensatory mechanisms. To improve our understanding of this understudied

373 splicing factor, we combined rapid depletion with nascent RNA sequencing (Nascent-

374 seq) (Radle et al., 2013; Schwalb et al., 2016). Nascent-seq captures only changes that

occur in newly transcribed RNAs and ignores the large fraction of pre-existing nuclear and cytoplasmic RNAs that would mask these changes. Especially at early time points, only a small number of differentially expressed or alternatively spliced targets are expected.

Homozygously tagged HeLa SRSF5-endo-GFP cells (**Figure S3D**) were induced with DOX and, at different time points (2, 8, and 16 h; termed T2, T8, and T16, respectively), were treated for one hour with 400 µM 4-thio-uridine (4sU), which is incorporated into newly transcribed RNAs (**Figure 6A**). Uninduced cells were used as controls, and SRSF5 depletion was controlled by Western blot (**Figure S5B**). After total RNA extraction, nascent transcripts with incorporated 4sU were biotinylated *in vitro*, purified using streptavidin-coated beads and converted into a strand-specific cDNA library (**Figure 6A, S5C**). 40% of uniquely mapped reads corresponded to intronic regions, in line with an enrichment of nascent, incompletely spliced pre-mRNAs. Surprisingly, differential expression analysis using DESeq2 (Love et al., 2014) uncovered very rapid and dynamic changes in gene expression after SRSF5 depletion (**Figure 6B, 6C; Table S1**). At T2, already 436 genes were differentially expressed (**Figure 6B**). Of those, 127 were exclusively regulated at T2, whereas 178 differentially expressed genes (DEGs) changed over the entire time-course. Interestingly, at T2, 87% of all DEGs were down-regulated (**Figure S5D**). Among them were 106 (28%) long non-coding RNAs (lncRNAs; **Figure 6C**). 50% of the down-regulated lncRNAs remained reduced until T16, while 40% were no longer regulated and 10% were even upregulated at T16 (**Figure 6C**). T8 showed the highest number of DEGs (2,531) with 1,766 exclusively regulated genes at this timepoint, while at T16, the number of DEGs was reduced again to 1,079, with 298 exclusively regulated genes (**Figure 6B**). This suggests that at longer SRSF5 depletion times, changes in gene expression are attenuated or overshoot due to compensatory mechanisms. In line with this, we identified very few DEGs upon siRNA-mediated SRSF5 KD (48 h) in P19 cells (Müller-McNicoll et al., 2016).

SRSF5 binds preferentially to down-regulated transcripts

404   To test whether down-regulated transcripts are bound by SRSF5, we performed

405   iCLIP2 (Buchbender et al., 2020) with HeLa hGRAD SRSF5-endo-GFP cells (5 replicates;

406   Figure S5E, S5F). We identified 415,245 reproducible SRSF5 binding sites in 8,280

407   protein-coding genes, mainly in coding regions and 5'UTRs, and 708 lncRNAs (Figure

408   S5G, S5H). Interestingly, 51% of the transcripts down-regulated at T2 contained SRSF5

409   binding sites compared to 15% in unregulated and 16.1% in up-regulated transcripts. A

410   similar trend was observed for the other timepoints (Figure S5J), suggesting that those

411   are direct targets of SRSF5. Among the bound transcripts, down-regulated transcripts

412   tended to have more SRSF5 binding sites than up-regulated transcripts (0.77 vs 0.21;

413   Figure S5J). For example, the lincRNAs *LINC01895, BASP1-AS, ENSG00000231412* and

414   *ENSG00000259621* were extensively bound by SRSF5 and showed decreased levels at all

415   three timepoints (Figure S5I, S5K). Similarly, *SRSF2* mRNA was decreased and highly

416   bound by SRSF5 (Figure S5K).

417   Unexpectedly, another mRNA that was strongly bound by SRSF5 and

418   downregulated at T8 and T16 was the *SRSF5* transcript itself. We expected its mRNA

419   levels to rise upon depletion of the SRSF5 protein, since SRSF5 auto-regulates its own

420   mRNA levels via splicing of a poison cassette exon (PCE), similar to other SR proteins

421   (Müller-McNicoll et al., 2019). RT-qPCR confirmed that *SRSF5* transcript levels

422   decreased to 50% and remained low even at 32 h of SRSF5 depletion (Figure 6D). SRSF5

423   bound most strongly in a region surrounding the *SRSF5* PCE, suggesting that SRSF5

424   binding normally regulates PCE inclusion (Figure 6E). In line with this, quantification of

425   PCE junctions revealed a decrease in PCE inclusion after 8 and 16 h SRSF5 depletion

426   from 10% to 4% (Figure S6A). This meant that the levels of *SRSF5-PCE* isoforms

427   decreased, while those of translatable *SRSF5* isoforms increased at T16, which may

428   counteract degradation of SRSF5. Apart from *SRSF2* and *SRSF5*, other SR protein

429   encoding mRNAs did not change upon SRSF5 depletion. However, we observed an

430   increase in PCE inclusion at T16 for SRSF3 (from 50.3 to 55.3%), SRSF6 (from 38.3 to

431   47.7%) and SRSF7 (from 63.5 to 69.7%; Figures S6B-D). Fewer translatable isoforms of

432   these SR proteins may contribute to the observed compensatory effects at longer

433　depletion times. Our data indicate that auto- and cross-regulation via PCE inclusion also

434　operate when SR protein levels are too low.

435　　　But what causes the early decrease in the levels of *SRSF5* mRNA and other

436　transcripts? SRSF5 could promote their transcription, splicing, 3'end processing and/or

437　stability. Since the sudden decrease in *SRSF5* mRNA levels was also detectable with

438　total RNA (**Figure 6D**), which is dominated by 'old' transcripts, reduced transcription

439　could be ruled out. To test whether SRSF5 depletion caused intron retention (IR) or

440　intronic polyadenylation, we analyzed the Nascent-seq data with IRFinder (Lorenzi et

441　al., 2021). We identified 181 significant IR events at timepoint T2, 717 events at T8, and

442　142 events at T16 (**Table S1**). However, only 1.1% of the down-regulated transcripts

443　showed IR at T2 (7.1% at T8, 1.4% at T16), and there was no evidence for premature

444　polyadenylation. This suggests that IR is not the main cause of decreased transcript
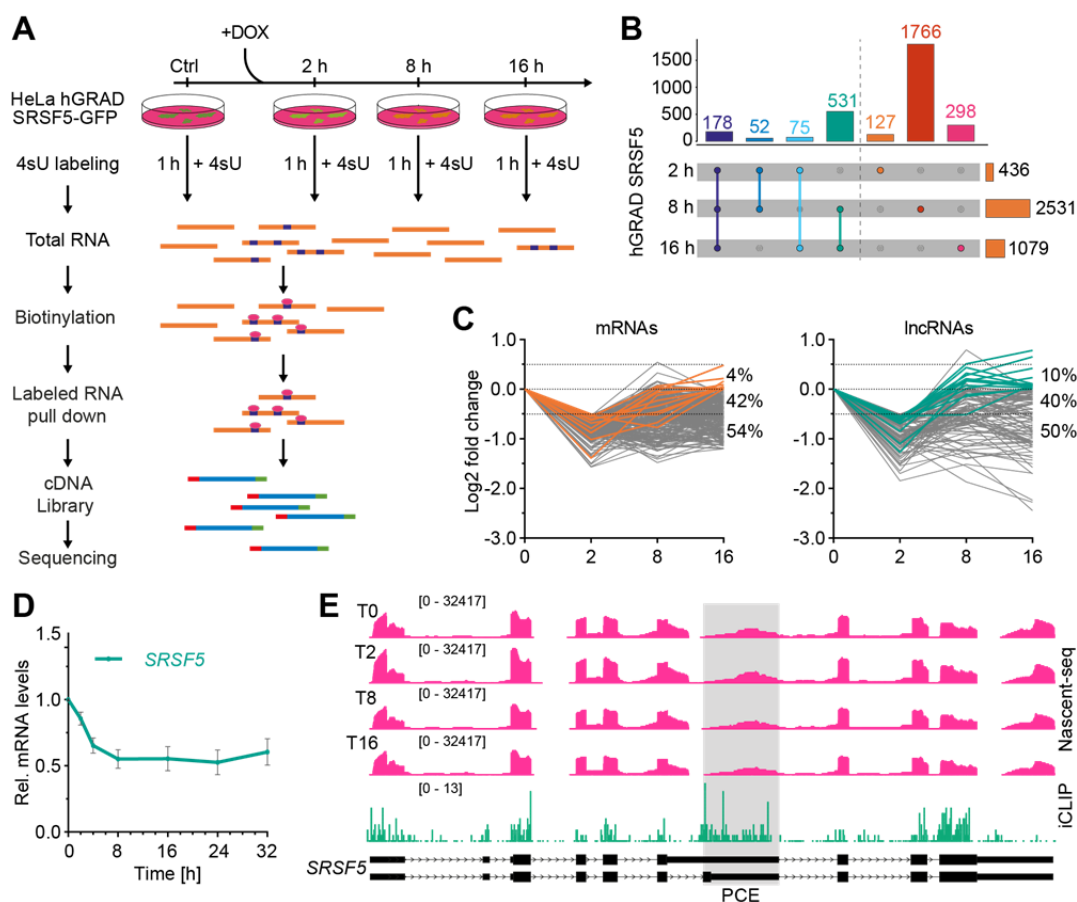
445　levels.

446

Figure 6. Combining hGRAD with Nascent-seq and iCLIP2 allows the identification of direct SRSF5 targets and reveals a function of SRSF5 in transcript stability. A) Scheme of the workflow combining a time-course of hGRAD degradation with Nascent-seq. Cells were first induced with DOX (1 μg/mL) for the indicated times. All new transcripts were labeled by addition of 4sU (400 μM) to the medium for one hour. Subsequently, total RNA was extracted, biotinylated, purified and converted into a cDNA library for deep sequencing. **B)** UpSet plot of differentially expressed transcripts. **C)** Rapid depletion of SRSF5 by hGRAD leads to dynamic changes in the abundance of mRNAs (left) and lncRNAs (right). All RNAs that are down-regulated at T2 are shown in grey. Transcripts that are compensated at T16 are highlighted in orange (mRNAs) or green (lncRNAs). **D)** RT-qPCR shows that *SRSF5* mRNA decreases until 8 h degradation and remains low until 32 h post-induction. Graph shows mean and SD of n=3 independent experiments. **E)** *SRSF5* transcripts show extensive SRSF5 binding but no processing alterations after SRSF5 depletion. Genome browser view showing Nascent-seq and SRSF5 iCLIP2 crosslinks on the *SRSF5* gene.

We speculated that *SRSF5-PCE* isoforms and other non-coding transcripts might decrease in abundance after acute SRSF5 depletion, because SRSF5 normally binds and targets them to nuclear speckles, which may protect them from nuclear decay machineries. To test this, we combined SRSF5 hGRAD depletion with RNA fluorescence *in situ* hybridization (FISH). We found that *SRSF5-PCE* transcripts accumulated in a bright spot that co-localized with SRSF5 and the nuclear speckle marker SRRM2 (**Figure S6E**). Interestingly, after 6 h of SRSF5 depletion *SRSF5-PCE* transcript levels were strongly decreased, the bright spots were completely dispersed and co-localization with nuclear speckles was no longer observed (**Figure S6E**). This suggest that acute SRSF5 degradation may release *SRSF5-PCE* transcripts from nuclear speckles and destabilize them, while normal SRSF5 isoforms are not affected and thus their relative levels increase. Based on the rapid decline of many other non-coding transcripts at 2 h after SRSF5 depletion, the preferential binding of SRSF5 to these transcripts and the absence of splicing alterations, we propose that SRSF5 binds and targets those transcripts to nuclear speckles to protect them from decay.

Our study demonstrates the usefulness of hGRAD to study the role of nuclear condensates in gene expression and discover novel functions of nuclear RBPs by distinguishing direct from indirect or compensatory effects.

479 **Discussion**

480

481   Studying the functions of individual RBPs is a challenging task. This is due to

482 similar domain structure, redundant functions, cooperation and competition for binding

483 sites and large networks of auto- and cross-regulation (Leclair et al., 2020; Meinke et al.,

484 2020; Sliskovic et al., 2022). Moreover, their high mRNA translation rates and protein

485 stability require long depletion times when using RNAi, which causes indirect effects

486 (Chen et al., 2018). To discriminate between the functions of individual SR proteins, we

487 and others have used endogenous GFP-tagging by CRISPR/Cas9. Here, we introduce a

488 simple system that allows the inducible, rapid and efficient depletion of such GFP-

489 tagged RBPs through genomic integration of a single plasmid. We show that our system,

490 termed hGRAD, can deplete various GFP-tagged proteins expressed in different cell

491 types and localizing to different subcellular compartments, including nuclear

492 condensates such as nuclear speckles and paraspeckles. hGRAD is more efficient, less

493 toxic and requires less extensive genome editing than comparable approaches like the

494 AID and Trim-Away systems.

495   hGRAD is derived from the deGradFP system, which was designed for

496 degradation of GFP-tagged proteins in *Drosophila* (Caussinus et al., 2011). Several reports

497 indicated that it is not suitable for the depletion of nuclear proteins in mammalian cells

498 (Daniel et al., 2018; Li et al., 2019). To improve this, we exchanged the F-box domain

499 from *Drosophila* Slmb for that of its human orthologue FBXW11. A similar approach

500 named zGRAD was shown to strongly increase degradation efficiency in zebrafish

501 (Yamaguchi et al., 2019). hGRAD achieved a similar degradation efficiency compared to

502 deGradFP and a significantly faster depletion than zGRAD.

503   Compared to the auxin-inducible systems osTIR1 and aaAFB2 and to TRIM-

504 away, hGRAD did not impair cell proliferation upon induction. This is likely because

505 the other approaches require the constitutive expression of large (70-90 kDa)

506 heterologous E3-Ub-ligases in order to be efficient (Clift et al., 2017; Daniel et al., 2018; Li

507 et al., 2019), which contain additional enzymatic domains, making potential off-target

508 effects more likely.   The osTIR1 and aaAFB2 systems showed a faster onset of

509 depletion with half-lives down to 25 min (Daniel et al., 2018), because all required

510 protein components are already expressed prior to induction with auxin. Moreover, a

511 fast recovery of the target protein can be achieved after auxin removal (Daniel et al.,

512 2018; Li et al., 2019). hGRAD has a longer onset and does not allow target protein

513 recovery similar to the deGradFP and zGRAD systems (Caussinus et al., 2011;

514 Yamaguchi et al., 2019). This might be due to the high stability of the nanobody fusions

515 and the single layer of induction via DOX addition. However, the osTIR1 system is

516 intrinsically leaky and led to a significant degradation of SRSF3 prior to auxin addition,

517 supporting other reports (Li et al., 2019). Moreover, the continuously expressed AID-

518 nanobody possibly binds to GFP-tagged proteins and alters or inhibit their functions,

519 which might contribute to the observed cytotoxic side effects.

520   Using hGRAD, we were able to almost completely deplete the nuclear speckle

521 protein SRSF5 after 3 h, which otherwise requires long depletion times by RNAi. This

522 allowed us to study its immediate effects with minimized compensation and cross-

523 regulation. The combination of hGRAD with Nascent-seq uncovered highly dynamic

524 transcript changes after SRSF5 depletion. Interestingly, these changes were transient in

525 nature and already appeared much attenuated at 16 h, which illustrates the robustness

526 of gene expression through compensatory mechanisms likely by other SR proteins.

527 Indeed, we discovered that SRSF5 depletion alters the inclusion levels of its own PCEs as

528 well as that of other SR proteins, indicating that auto- and cross-regulation operate when

529 SRSF5 levels are too low. Moreover, our data suggest a novel role for SRSF5 in transcript

530 stability, whereby SRSF5 binding targets and stores *SRSF5-PCE* transcripts and likely

531 other non-coding transcripts in nuclear speckles. Acute depletion of SRSF5 releases

532 bound transcripts from these condensates where they are now exposed to nuclear decay.

533 At later time points other SR proteins might bind and compensate for nuclear speckle

534 targeting so that transcript levels recover.

535   Rapid depletion is the tool of choice to study the functions of individual RBPs.

536 hGRAD now allows the rapid degradation of notoriously difficult to target nuclear RBPs

537 that localize to condensates. It allows to disentangle protein functions from those of

538 transcripts that are produced from the same genomic locus, to study auto- and cross-

539 regulation and it allows to study the role of condensates in the regulation of gene

540 expression. Our 'one-fits-all' system can be inserted by a one-step procedure in any cell

541 expressing GFP-tagged proteins, often commercially available and functionally

542 validated. Moreover, the hGRAD vector is flexible and the F-box domain could be

543 replaced with other targeting moieties or enzymatic activities, e.g. APEX2 for proximity

544 labelling or kinases to modify GFP-tagged proteins in a rapid and inducible manner,

545 making it a very useful tool for future studies.

546

Acknowledgements

555

Author contributions

557 BA and MMM designed the experiments. BA, RJR, FM and EKO performed the

558 experiments. BA, RJR, IS, MK and KZ performed the analyses. Figures were prepared by

559 BA and RJR. The manuscript was written by BA, RR, KZ and MMM.

560

Competing Interests Statement

562 The authors declare no competing interests.

563

Data availability

565 All sequencing data is available in the Gene Expression Omnibus (GEO) under the

566 SuperSeries accession number GSE229326. The collection includes the Nascent-seq data

567 of SRSF5-GFP-endo (GSE229324) as well as the iCLIP data for SRSF5-GFP-endo in HeLa

568 cells (GSE229325). The token for anonymous reviewer access is ejsfsuaoxrkdfwh

569 at: https://www.ncbi.nlm.nih.gov/geo/query/acc.cgi?acc=GSE229326

Material and Methods

Generation of plasmid constructs

The pTRE-BI-hGRAD, -TRIM21, -aaAFB2 and -osTIR1 plasmids were generated by Gibson assembly (GBA). For this a DOX-inducible bi-directional pTRE-BI vector was designed and synthesized by VectorBuilder (Vector ID: VB190904-1039fwc). For the pTRE-BI-hGRAD plasmid, a sequence encoding mCherry was added on one side of the tet-inducible bi-directional promoter by conventional restriction cloning (*Bam*HI & *Spe*I; New England Biolabs). The coding region of a human F-box domain (215 amino acids [aa], UniProt ID: Q9UKB1) fused to the sequence of an anti-GFP nanobody (VHH-GFP4) (Saerens et al., 2005) was inserted on the other side by GBA. For the pTRE-BI-TRIM21 plasmid, the pTRE-BI vector was linearized with *Bam*HI and *Nhe*I (New England Biolabs) and inserts were integrated by GBA. The sequences encoding TRIM21 (476 aa, UniProt ID: P19474) fused to mCherry and a weak NLS signal (AAAKRVKLD) (Li et al., 2019) was inserted at one side of the tet-inducible bi-directional promoter and the human IgG1 Fc2 domain was inserted at the other side. For pTRE-BI-osTIR1, the *osTIR1* gene (574 aa, UniProt ID: Q7XVM8) fused to mCherry and a weak NLS signal was inserted at one side of the bi-directional promoter and the mAID sequence (Daniel et al., 2018) and the GFP nanobody (VHH-GFP4) was added to the other side. For pTRE-BI-aaAFB2, the *aaAFB2* gene (575 aa, UniProt ID: Q9LW29) fused to mCherry and a weak NLS signal was inserted at one end of the bi-directional promoter and the miniIAA7 AID sequence (Li et al., 2019) and the GFP nanobody (VHH-GFP4) to the other side.

Plasmids used as circular homology directed repair (HDR) templates were generated by GBA. 1-kb homology arms flanking the single guide RNA (sgRNA) cut sites were amplified by PCR from host genomic DNA with primers containing overlapping sequences. The GFP-Neo® resistance cassette containing a GFP-tag, the Neomycin (Neo®) resistance gene and an internal ribosome entry site (IRES) was amplified from the SRSF3 BAC DNA (Müller-McNicoll et al., 2016). PCRs were performed with either S7 Fusion Polymerase™ (Mobidiag), Q5® High-Fidelity or Taq DNA Polymerases (both New

598   England Biolabs). PCR inserts and linearized pGEM®-T Easy vector (Promega) were

599   combined by GBA performed with Taq DNA Ligase and T5 Exonuclease (both New

600   England Biolabs). One Shot™ TOP10 chemically competent *E. coli* cells (Invitrogen) were

601   used for transformations. Plasmids were extracted from bacteria with the ZR Plasmid

602   Miniprep Classic (Zymo Research). Successful cloning was confirmed by Sanger

603   sequencing (ACGT). All plasmids are listed in **Table S4** and all primers in **Table S7**.

604   *Generation of stable cell lines and drug treatments*

605   For integration of the pTRE-BI vectors, WT HeLa and P19 cells were transfected with 0.8

606   µg purified and linearized plasmid DNA per well in 6-well plates using the jetPRIME®

607   Transfection reagent (Polyplus-transfection). Cells with stably integrated plasmids were

608   selected with 2 µg/mL puromycin (Gibco™, Thermo Fisher Scientific). Single cell clones

609   were generated by limited dilution, grown from single cells in 96-well plates and

610   screened for high inducibility by confocal microscopy upon DOX-induction (1 µg/mL).

611   Bacterial artificial chromosomes (BAC) harboring sequences encoding for C-terminally

612   GFP-tagged *SRSF3, SRSF5, NONO, EIF4E* and *SRPK1* genes (**Table S5**) were isolated

613   from *E. coli* DH10 cells using the NucleoBond™ Xtra Midi EF kit. For integration of the

614   BACs WT HeLa and P19 cells were transfected with 1 µg purified BAC DNA per well in

615   6-well plates using jetPRIME®. Cells with stably integrated BACs were selected with

616   400 µg/mL Geneticin™ (G418, Gibco™, sorted for single cell clones with near-

617   endogenous expression levels and expanded. All stable cell lines are listed in **Table S6**.

618   HeLa and P19 cells were cultivated under humidified condition at 5% CO_2 and 37 °C in

619   DMEM GlutaMAX Medium, supplemented with 10% (v/v) heat inactivated fetal bovine

620   serum and 100 µg/mL penicillin-streptomycin (all Gibco™, Thermo Fisher Scientific).

621   Live cells were counted with an EVE™ Automated Cell Counter device (NanoEnTek

622   Inc). For this, equal volumes of cell suspension and 0.4% (v/v) trypan blue stain solution

623   (Gibco™, Thermo Fisher Scientific) were mixed and applied to EVE™ Cell counting

624   slides. To inhibit the proteasome, HeLa cells were grown on coverslips placed in 24-well

625   plates and treated with 10 µM of MG132 (M7449-200UL, Sigma Aldrich) diluted in fresh

626　DMEM for 4 h followed by fixation with 4% PFA (Thermo Fisher Scientific). To induce

627　expression of the hGRAD and TRIM21 systems, cells were treated with 1 µg/mL

628　doxycyclin (DOX; Sigma-Aldrich, D9891). osTIR1 and aaAFB2-expressing cells were

629　additionally treated with 0.5 mM auxin (AUX; Sigma Aldrich, I2886-25G).

630　*Genome editing with CRISPR/Cas9*

631　For endogenous C-terminal tagging of *SRSF3*, *SRSF5* and *SRRM2*, single guide RNAs

632　(sgRNAs) were designed using CRISPOR (http://crispor.tefor.net) and purchased from

633　IDT (Integrated DNA Technologies). HeLa and P19 cells were first transfected with

634　circular HDR donor plasmids comprising the GFP-Neo® resistance cassette flanked by

635　gene-specific 1-kb homology arms (HA) using jetPRIME® (Polyplus). After 6-12 h, WT

636　cells were transfected with pre-assembled sgRNAs (Alt-R® CRISPR-Cas9 crRNA (target-

637　specific, see **Table S2**) and Alt-R® CRISPR-Cas9 tracrRNA Atto550 labeled, IDT) and

638　recombinant Cas9 protein (Alt-R® *S. p.* HiFi Cas9 Nuclease V3, IDT) using

639　Lipofectamine™ CRISPRMAX (Invitrogen) and cultured for 48 h in the presence of an

640　HDR enhancer (final concentration 20 µM, IDT). Cells were then selected with

641　Geneticin® (Gibco, 400 µg/mL). CRISPR clones were generated by limited dilution and

642　grown from single cells in 96-well plates. For genomic screening, cells were washed

643　twice with PBS in the 96-well plates and lysed in directPCR buffer (20 mM Tris-HCl, pH

644　8, 200 mM NaCl, 1 mM EDTA, 0.5% Tween-20, 0.5% NP-40) with freshly added 200

645　µg/mL Proteinase K (Sigma Aldrich), and incubated for 1 h at 55°C followed by

646　Proteinase K inactivation at 95 °C for 15 min. Screening PCRs were performed from

647　crude lysates using primers flanking the edited region. Sequences of the gRNAs are

648　shown in **Table S2** and primers in **Table S7**.

649　*RNA isolation, reverse transcription and qPCR*

650　Cells were harvested and resuspended in TRIzol™ (Thermo Fisher Scientific). RNA was

651　extracted according to the manufacturer's instructions, treated with TURBO™ DNase

652　(Thermo Fisher Scientific) for 30 min at 37 °C to remove genomic DNA and

653　subsequently purified. Two µg of RNA were reverse transcribed into cDNA using

654   SuperScript™ and 10 mM dNTP Mix (both Thermo Fisher Scientific) and oligodT (Sigma

655   Aldrich).   qPCR   primers   were   selected   using   Primer-BLAST

656   (https://www.ncbi.nlm.nih.gov/tools/primer-blast/).   qPCRs   were   performed   using

657   cDNA (1:8 dilution) and the ORA™ SEE qPCR Green ROX L kit (highQu) on a PikoReal

658   96 machine (Thermo Fisher Scientific). GraphPad Prism was used for graphics/statistics.

659   Primers used are listed in Table S7.

660   *Western blot and antibodies*

661   Cells were lysed in 300 µl NET-2 buffer (150 mM NaCl, 0.05% (v/v) NP-40, 50 mM Tris-

662   HCl pH 7.5), supplemented with 1× cOmplete Protease Inhibitor Cocktail (Sigma

663   Aldrich) and 10 mM β-phosphoglycerate (Fluka BioChemica) or with RIPA buffer (150

664   mM NaCl, 0.05% (v/v) NP-40, 50 mM Tris-HCl pH 7.5, 0.1% (w/v) SDS, 0.5% (w/v)

665   sodium deoxycholate, freshly added 1× cOmplete Protease Inhibitor Cocktail and 10 mM

666   β-phosphoglycerate). NET-2 lysates were sonicated on ice for 30 sec (3 pulses of 10 sec;

667   20 sec intervals) at 20% amplitude (Branson W-450 D) and cleared by centrifugation.

668   Protein concentrations were measured using Quick Start Bradford 1× Dye Reagent (Bio-

669   Rad®) on a NanoDrop2000 (Thermo Fisher Scientific) or DC Protein-Assay (Bio-Rad®) for

670   RIPA samples. 20-40 µg protein were separated by SDS-PAGE on 4-15% Mini-

671   PROTEAN® TGX Stain-Free™ Gels (Bio-Rad®). and transferred onto PVDF membranes

672   using Trans-Blot Turbo RTA Mini LF PVDF Transfer Kit (Bio-Rad®). Transfer and equal

673   loading were evaluated by activation of stain-free gels by UV light. Membranes were

674   probed with the antibodies listed in Table S3. Proteins were imaged using secondary

675   antibodies coupled to a horseradish peroxidase and Amersham™ ECL Prime Western

676   Blotting Detection Reagent (Cytiva) with the ChemiDoc™ MP Imaging System. Image

677   quantification was performed using the ImageLab software (Bio-Rad).

678   *GFP fluorescence microscopy and live-cell imaging*

679   For GFP fluorescence microscopy, cells were grown on 10 mm glass coverslips. After

680   removing the medium cells were gently washed twice with DPBS and fixed with 4%

681   PFA (Thermo Fisher Scientific) in PBS for 10 min at RT. DNA was stained with Hoechst

682   34580 (1:4000, in TBST; Thermo Fisher Scientific). After a final wash, the coverslips were

683   dried and mounted on ProLong™ Diamond Antifade Mountant (Invitrogen). All

684   microscopy experiments were visualized using a Zeiss LSM780 confocal microscope

685   system and Zen Black imaging software.

686   For live-cell imaging, cells were incubated in a microscopy grade 24-well glass-bottom

687   culture plate (Sensoplate, Greiner Bio-ONE). Prior to imaging, the medium was

688   exchanged with low autofluorescent FluoroBrite™ DMEM Media (Gibco) supplemented

689   with 10% (v/v) FBS, 2 mM GlutaMAX ™ I Supplement and 1 mM sodium pyruvate (all

690   Gibco™, Thermo Fisher Scientific). 100 nM SiR-DNA stain (Spirochrome) was added for

691   the visualization of nuclei. Cell culture plates were mounted on Zeiss LSM 780

692   microscope, equipped with a humidified incubation chamber (pre-heated for 2 hours at

693   37 °C, 5% CO_2). Selected regions were automatically imaged every 15-20 minutes with

694   pre-set settings and software autofocus using the ZEN Black software. GFP intensity and

695   SiR-DNA were visualized in parallel. Eight Z-stacks per region with a slice thickness of 2

696   µm were imaged. To minimize phototoxicity, minimal possible laser intensity was

697   chosen (488 nm <3%, 670; 633 nm <5%). GFP intensity changes in individual cells were

698   quantified over time using Fiji software (Schindelin et al., 2012) and the TrackMate

699   plugin (Tinevez et al., 2017). First, a Z-maximum intensity projection was made to

700   generate a single plane image. The background was subtracted using a rolling ball

701   background subtraction algorithm with a disk size of 75 µm. TrackMate was first

702   applied to the SiR-DNA channel to identify and connect cell tracks over time. The mean

703   GFP intensity was evaluated in corresponding cells and normalized to the first time

704   point.

705   *4sU treatment and nascent RNA sequencing*

706   HeLa cells were treated with 400 µM 4-thio-uridine (4sU, Sigma Aldrich) for 1 hour to

707   label freshly transcribed RNAs. The reaction was stopped by applying TRIzol™RI

708   reagent to the culture dishes. RNA extraction and pulldown of newly transcribed RNA

709   was performed according to (Gressel et al., 2019) without fractionation of the RNA by

710   sonification. Nascent RNA was purified using RNA Clean and Concentrate Kit

711   (ZymoResearch). cDNA libraries for RNA-seq were prepared with universal Plus™

712   Total RNA-Seq Library Preparation Kit (Tecan) according to manufacturer's instructions.

713   Ribosomal RNA fragments were removed and the library was sequenced on an Illumina

714   NovaSeq6000 instrument (2 replicates per timepoint, 100 Mio reads, 150 bp, paired-end).

715   Reads were mapped to the human genome (hg38) using the STAR mapper (version

716   2.7.10) (Dobin et al., 2013) with the following parameters: --outFilterMultimapNmax 1 --

717   outFilterMismatchNmax 999 --outFilterMismatchNoverReadLmax 0.04 --outSAMtype

718   BAM SortedByCoordinate.

719   To quantify IR events, IRFinder (version 1.3.1) (Middleton et al., 2017) was used with

720   default parameters. Differential gene expression was quantified using DESeq2 with

721   default parameters (Love et al., 2014). Sashimi plots for poison cassette exons of selected

722   SR proteins were prepared using the R/Bioconductor package Gviz (version 1.37.2) by

723   taking the merged BAM files of each timepoint as input. Junctions were filtered for the

724   junctions describing the inclusion levels of the poison cassette exons.

725

726   *iCLIP2 libraries*

727   iCLIP experiments were performed using the iCLIP2 protocol (Buchbender et al., 2020)

728   with minor modifications. For each replicate, cells were grown near confluence on two

729   150-mm culture dishes, washed with ice-cold PBS, irradiated with 150 mJ/cm² UV light

730   at 254 nm (CL-1000, UVP), harvested by scraping and centrifugation and stored at -80°C

731   until lysis. Following lysis and partial digestion with RNase I (Thermo Fisher Scientific,

732   AM2294), immunoprecipitation of SRSF5-GFP was performed using a goat anti-GFP

733   antibody (MPI-CBG, Dresden, Germany) coupled to Dynabeads™ Protein G (Thermo

734   Fisher Scientific, 10002D). Co-purified, crosslinked RNA fragments were

735   dephosphorylated at their 3′ ends using T4 Polynucleotide Kinase (New England

736   Biolabs, M0201S) and ligated to a pre-adenylated 3′ adapter (L3-App). To visualize

737   protein-RNA complexes, RNA fragments crosslinked to SRSF5-GFP were labeled at their

31

738 5′ ends using T4 Polynucleotide Kinase and γ-^{32}P ATP (Hartmann Analytic). Samples

739 were run on a Nu-PAGE 4-12% Bis-Tris Protein Gel (Thermo Fisher Scientific,

740 NP0335BOX), transferred to a 0.45 μm nitrocellulose membrane (GE Healthcare Life

741 Science, 10600002) and visualized using a Phosphorimager. Regions of interest were cut

742 from the nitrocellulose membrane (70 kDa to 130 kDa) and RNA was released from the

743 membrane using Proteinase K (Roche, 03115828001). RNA was purified using neutral

744 phenol/chloroform/isoamylalcohol (Ambion, AM9722) followed by chloroform (Serva,

745 39554.02) extraction, and reverse transcribed using SuperScript III™ (Life Technologies,

746 18080-044). cDNA was cleaned up using MyONE Silane beads (Life Technologies,

747 37002D) followed by ligation of a second adapter containing a bipartite (5-nt + 4-nt)

748 unique molecular identifier (UMI) as well as a 6-nt experimental barcode (Buchbender et

749 al., 2020). iCLIP2 libraries were pre-amplified with 6 PCR cycles using short primers

750 (P5Solexa_short and P3Solexa_short) and then size-selected using the ProNex Size-

751 Selective Purification System (Promega, NG2001) in a 1:2.95 (v/v) sample:bead ratio to

752 eliminate products originating from short cDNAs or primer dimers. The size-selected

753 library was amplified for 6 cycles using P5Solexa and P3Solexa primers, and primers

754 were removed using the ProNex Size-Selective Purification System (Promega, NG2001)

755 in a 1:2.4 (v/v) sample:bead ratio. Purified iCLIP2 libraries were sequenced on a

756 NextSeq500 System (Illumina) using a NextSeq® 500/550 High Output Kit v2 as 92-nt

757 single-end reads including a 6-nt sample barcode as well as 5+4-nt UMIs yielding between

758 5.4 and 74.1 million reads.

759 *iCLIP2 analysis*

760 Basic quality controls were done using FastQC (version 0.11.8)

761 (https://www.bioinformatics.babraham.ac.uk/projects/fastqc/). The FASTX-Toolkit (version

762 0.0.14) (http://hannonlab.cshl.edu/fastx_toolkit/) and seqtk (version 1.3)

763 (https://github.com/lh3/seqtk/) were used to filter reads based on sequencing qualities

764 (Phred score) in the barcode and UMI regions. Read were de-multiplexed according to the

765 sample barcode on positions 6 to 11 of the reads using Flexbar (version 3.4.0, using non-

766 default parameter --barcode-keep) (Roehr et al., 2017). Flexbar was also used to trim UMI

767 and barcode regions as well as adapter sequences from read ends requiring a minimal

768 overlap of 1 nt of read and adapter. UMIs were added to the read names and reads shorter

769 than 15 nt were removed from further analysis. The downstream analysis was done as

770 described in Chapters 3.4 and 4 of (Busch et al., 2020) with an additional step to remove

771 reads directly mapped to the chromosome ends using Samtools (version 1.9) (Danecek et al.,

772 2021) and bedtools (version 2.27.1) (Quinlan and Hall, 2010). Those reads do not have an

773 upstream position and, thus, no crosslink position can be extracted. Genome assembly and

774 annotation of GENCODE (release 31) (Frankish et al., 2019) were used during mapping with

775 STAR (version 2.7.3a) (Dobin et al., 2013).

776 Processed reads from five replicates were merged prior to peak calling with PureCLIP

777 (version 1.3.1) (Krakau et al., 2017) using a minimum transition probability of 1%.

778 Significant crosslink sites (1 nt) were filtered by their PureCLIP score, removing the

779 lowest 2% of crosslink sites. The remaining sites were merged into 7-nt wide binding

780 sites using the R/Bioconductor package BindingSiteFinder (version 1.0.0), filtering for

781 sites with at least 3 positions covered by crosslink events. Binding sites were overlapped

782 with gene and transcript annotations obtained from GENCODE (release 29). Binding

783 sites within protein-coding genes were assigned to the transcript regions, i.e., intron,

784 CDS, 3'UTR or 5'UTR.

785

References

787 Beghein, E., and J. Gettemans. 2017. Nanobody Technology: A Versatile Toolkit for Microscopic Imaging,
788 Protein-Protein Interaction Analysis, and Protein Function Exploration. *Front Immunol*. 8:771.
789 Buchbender, A., H. Mutter, F.X.R. Sutandy, N. Kortel, H. Hanel, A. Busch, S. Ebersberger, and J. König. 2020.
790 Improved library preparation with the new iCLIP2 protocol. *Methods*. 178:33-48.
791 Busch, A., M. Brüggemann, S. Ebersberger, and K. Zarnack. 2020. iCLIP data analysis: A complete pipeline
792 from sequencing reads to RBP binding sites. *Methods*. 178:49-62.
793 Caussinus, E., and M. Affolter. 2016. deGradFP: A System to Knockdown GFP-Tagged Proteins. *Methods Mol
794 Biol*. 1478:177-187.
795 Caussinus, E., O. Kanca, and M. Affolter. 2011. Fluorescent fusion protein knockout mediated by anti-GFP
796 nanobody. *Nat Struct Mol Biol*. 19:117-121.
797 Chen, Y., Q. Huang, W. Liu, Q. Zhu, C.P. Cui, L. Xu, X. Guo, P. Wang, J. Liu, G. Dong, W. Wei, C.H. Liu, Z.
798 Feng, F. He, and L. Zhang. 2018. Mutually exclusive acetylation and ubiquitylation of the splicing factor
799 SRSF5 control tumor growth. *Nat Commun*. 9:2464.
800 Clift, D., W.A. McEwan, L.I. Labzin, V. Konieczny, B. Mogessie, L.C. James, and M. Schuh. 2017. A Method
801 for the Acute and Rapid Degradation of Endogenous Proteins. *Cell*. 171:1692-1706 e1618.

802 Danecek, P., J.K. Bonfield, J. Liddle, J. Marshall, V. Ohan, M.O. Pollard, A. Whitwham, T. Keane, S.A.
803 McCarthy, R.M. Davies, and H. Li. 2021. Twelve years of SAMtools and BCFtools. *Gigascience*. 10.
804 Daniel, K., J. Icha, C. Horenburg, D. Muller, C. Norden, and J. Mansfeld. 2018. Conditional control of
805 fluorescent protein degradation by an auxin-dependent nanobody. *Nat Commun*. 9:3297.
806 de Oliveira Freitas Machado, C., M. Schafranek, M. Brüggemann, M.C. Hernández Cañás, M. Keller, A. Di
807 Liddo, A. Brezski, N. Blümel, B. Arnold, A. Bremm, I. Wittig, N. Jaé, F. McNicoll, S. Dimmeler, K. Zarnack,
808 and M. Müller-McNicoll. 2023. Poison cassette exon splicing of SRSF6 regulates nuclear speckle dispersal
809 and the response to hypoxia. *Nucleic Acids Res*. 51:870-890.
810 Dobin, A., C.A. Davis, F. Schlesinger, J. Drenkow, C. Zaleski, S. Jha, P. Batut, M. Chaisson, and T.R.
811 Gingeras. 2013. STAR: ultrafast universal RNA-seq aligner. *Bioinformatics*. 29:15-21.
812 Franic, D., K. Zubcic, and M. Boban. 2021. Nuclear Ubiquitin-Proteasome Pathways in Proteostasis
813 Maintenance. *Biomolecules*. 11.
814 Frankish, A., M. Diekhans, A.M. Ferreira, R. Johnson, I. Jungreis, J. Loveland, J.M. Mudge, C. Sisu, J. Wright,
815 J. Armstrong, I. Barnes, A. Berry, A. Bignell, S. Carbonell Sala, J. Chrast, F. Cunningham, T. Di Domenico, S.
816 Donaldson, I.T. Fiddes, C. García Girón, J.M. Gonzalez, T. Grego, M. Hardy, T. Hourlier, T. Hunt, O.G.
817 Izuogu, J. Lagarde, F.J. Martin, L. Martínez, S. Mohanan, P. Muir, F.C.P. Navarro, A. Parker, B. Pei, F. Pozo,
818 M. Ruffier, B.M. Schmitt, E. Stapleton, M.M. Suner, I. Sycheva, B. Uszczynska-Ratajczak, J. Xu, A. Yates, D.
819 Zerbino, Y. Zhang, B. Aken, J.S. Choudhary, M. Gerstein, R. Guigó, T.J.P. Hubbard, M. Kellis, B. Paten, A.
820 Reymond, M.L. Tress, and P. Flicek. 2019. GENCODE reference annotation for the human and mouse
821 genomes. *Nucleic Acids Res*. 47:D766-D773.
822 Frescas, D., and M. Pagano. 2008. Deregulated proteolysis by the F-box proteins SKP2 and beta-TrCP:
823 tipping the scales of cancer. *Nat Rev Cancer*. 8:438-449.
824 Gebauer, F., T. Schwarzl, J. Valcarcel, and M.W. Hentze. 2021. RNA-binding proteins in human genetic
825 disease. *Nat Rev Genet*. 22:185-198.
826 Gressel, S., B. Schwalb, and P. Cramer. 2019. The pause-initiation limit restricts transcription activation in
827 human cells. *Nat Commun*. 10:3603.
828 Harmsen, M.M., and H.J. De Haard. 2007. Properties, production, and applications of camelid single-
829 domain antibody fragments. *Appl Microbiol Biotechnol*. 77:13-22.
830 Holland, A.J., D. Fachinetti, J.S. Han, and D.W. Cleveland. 2012. Inducible, reversible system for the rapid
831 and complete degradation of proteins in mammalian cells. *Proc Natl Acad Sci U S A*. 109:E3350-3357.
832 Ishii, M., and B. Akiyoshi. 2022. Targeted protein degradation using deGradFP in Trypanosoma brucei.
833 *Wellcome Open Res*. 7:175.
834 James, L.C., A.H. Keeble, Z. Khan, D.A. Rhodes, and J. Trowsdale. 2007. Structural basis for PRYSPRY-
835 mediated tripartite motif (TRIM) protein function. *Proc Natl Acad Sci U S A*. 104:6200-6205.
836 Jeong, S. 2017. SR Proteins: Binders, Regulators, and Connectors of RNA. *Mol Cells*. 40:1-9.
837 Jin, J., T. Cardozo, R.C. Lovering, S.J. Elledge, M. Pagano, and J.W. Harper. 2004. Systematic analysis and
838 nomenclature of mammalian F-box proteins. *Genes Dev*. 18:2573-2580.
839 Kipreos, E.T., and M. Pagano. 2000. The F-box protein family. *Genome Biol*. 1:REVIEWS3002.
840 Komander, D., and M. Rape. 2012. The ubiquitin code. *Annu Rev Biochem*. 81:203-229.
841 Königs, V., C. de Oliveira Freitas Machado, B. Arnold, N. Blümel, A. Solovyeva, S. Löbbert, M. Schafranek, I.
842 Ruiz De Los Mozos, I. Wittig, F. McNicoll, M.H. Schulz, and M. Müller-McNicoll. 2020. SRSF7 maintains its
843 homeostasis through the expression of Split-ORFs and nuclear body assembly. *Nat Struct Mol Biol*. 27:260-
844 273.
845 Leclair, N.K., M. Brugiolo, L. Urbanski, S.C. Lawson, K. Thakar, M. Yurieva, J. George, J.T. Hinson, A.
846 Cheng, B.R. Graveley, and O. Anczukow. 2020. Poison Exon Splicing Regulates a Coordinated Network of
847 SR Protein Expression during Differentiation and Tumorigenesis. *Mol Cell*. 80:648-665 e649.
848 Li, S., X. Prasanna, V.T. Salo, I. Vattulainen, and E. Ikonen. 2019. An efficient auxin-inducible degron system
849 with low basal degradation in human cells. *Nat Methods*. 16:866-869.
850 Lorenzi, C., S. Barriere, K. Arnold, R.F. Luco, A.J. Oldfield, and W. Ritchie. 2021. IRFinder-S: a
851 comprehensive suite to discover and explore intron retention. *Genome Biol*. 22:307.
852 Love, M.I., W. Huber, and S. Anders. 2014. Moderated estimation of fold change and dispersion for RNA-
853 seq data with DESeq2. *Genome Biol*. 15:550.

854 Ludwicki, M.B., J. Li, E.A. Stephens, R.W. Roberts, S. Koide, P.T. Hammond, and M.P. DeLisa. 2019. Broad-
855 Spectrum Proteome Editing with an Engineered Bacterial Ubiquitin Ligase Mimic. *ACS Cent Sci*. 5:852-866.
856 Meinke, S., G. Goldammer, A.I. Weber, V. Tarabykin, A. Neumann, M. Preussner, and F. Heyd. 2020. Srsf10
857 and the minor spliceosome control tissue-specific and dynamic SR protein expression. *Elife*. 9.
858 Middleton, R., D. Gao, A. Thomas, B. Singh, A. Au, J.J. Wong, A. Bomane, B. Cosson, E. Eyras, J.E. Rasko,
859 and W. Ritchie. 2017. IRFinder: assessing the impact of intron retention on mammalian gene expression.
860 *Genome Biol*. 18:51.
861 More, D.A., and A. Kumar. 2020. SRSF3: Newly discovered functions and roles in human health and
862 diseases. *Eur J Cell Biol*. 99:151099.
863 Müller-McNicoll, M., V. Botti, A.M. de Jesus Domingues, H. Brandl, O.D. Schwich, M.C. Steiner, T. Curk, I.
864 Poser, K. Zarnack, and K.M. Neugebauer. 2016. SR proteins are NXF1 adaptors that link alternative RNA
865 processing to mRNA export. *Genes Dev*. 30:553-566.
866 Müller-McNicoll, M., O. Rossbach, J. Hui, and J. Medenbach. 2019. Auto-regulatory feedback by RNA-
867 binding proteins. *J Mol Cell Biol*. 11:930-939.
868 Nakayama, K.I., and K. Nakayama. 2006. Ubiquitin ligases: cell-cycle control and cancer. *Nat Rev Cancer*.
869 6:369-381.
870 Nishimura, T., H. Nakano, K. Hayashi, C. Niwa, and T. Koshiba. 2009. Differential downward stream of
871 auxin synthesized at the tip has a key role in gravitropic curvature via TIR1/AFBs-mediated auxin signaling
872 pathways. *Plant Cell Physiol*. 50:1874-1885.
873 Quinlan, A.R., and I.M. Hall. 2010. BEDTools: a flexible suite of utilities for comparing genomic features.
874 *Bioinformatics*. 26:841-842.
875 Radle, B., A.J. Rutkowski, Z. Ruzsics, C.C. Friedel, U.H. Koszinowski, and L. Dolken. 2013. Metabolic
876 labeling of newly transcribed RNA for high resolution gene expression profiling of RNA synthesis,
877 processing and decay in cell culture. *J Vis Exp*.
878 Ratnadiwakara, M., M. Mohenska, and M.L. Anko. 2018. Splicing factors as regulators of miRNA biogenesis
879 - links to human disease. *Semin Cell Dev Biol*. 79:113-122.
880 Roehr, J.T., C. Dieterich, and K. Reinert. 2017. Flexbar 3.0 - SIMD and multicore parallelization.
881 *Bioinformatics*. 33:2941-2942.
882 Rothbauer, U., K. Zolghadr, S. Muyldermans, A. Schepers, M.C. Cardoso, and H. Leonhardt. 2008. A
883 versatile nanotrap for biochemical and functional studies with fluorescent fusion proteins. *Mol Cell*
884 *Proteomics*. 7:282-289.
885 Saerens, D., M. Pellis, R. Loris, E. Pardon, M. Dumoulin, A. Matagne, L. Wyns, S. Muyldermans, and K.
886 Conrath. 2005. Identification of a universal VHH framework to graft non-canonical antigen-binding loops of
887 camel single-domain antibodies. *J Mol Biol*. 352:597-607.
888 Schindelin, J., I. Arganda-Carreras, E. Frise, V. Kaynig, M. Longair, T. Pietzsch, S. Preibisch, C. Rueden, S.
889 Saalfeld, B. Schmid, J.Y. Tinevez, D.J. White, V. Hartenstein, K. Eliceiri, P. Tomancak, and A. Cardona. 2012.
890 Fiji: an open-source platform for biological-image analysis. *Nat Methods*. 9:676-682.
891 Schulman, B.A., A.C. Carrano, P.D. Jeffrey, Z. Bowen, E.R. Kinnucan, M.S. Finnin, S.J. Elledge, J.W. Harper,
892 M. Pagano, and N.P. Pavletich. 2000. Insights into SCF ubiquitin ligases from the structure of the Skp1-Skp2
893 complex. *Nature*. 408:381-386.
894 Schwalb, B., M. Michel, B. Zacher, K. Fruhauf, C. Demel, A. Tresch, J. Gagneur, and P. Cramer. 2016. TT-seq
895 maps the human transient transcriptome. *Science*. 352:1225-1228.
896 Shin, Y.J., S.K. Park, Y.J. Jung, Y.N. Kim, K.S. Kim, O.K. Park, S.H. Kwon, S.H. Jeon, A. Trinh le, S.E. Fraser,
897 Y. Kee, and B.J. Hwang. 2015. Nanobody-targeted E3-ubiquitin ligase complex degrades nuclear proteins.
898 *Sci Rep*. 5:14269.
899 Sliskovic, I., H. Eich, and M. Müller-McNicoll. 2022. Exploring the multifunctionality of SR proteins. *Biochem*
900 *Soc Trans*. 50:187-198.
901 Tinevez, J.Y., N. Perry, J. Schindelin, G.M. Hoopes, G.D. Reynolds, E. Laplantine, S.Y. Bednarek, S.L. Shorte,
902 and K.W. Eliceiri. 2017. TrackMate: An open and extensible platform for single-particle tracking. *Methods*.
903 115:80-90.
904 Trost, M., A.C. Blattner, and C.F. Lehner. 2016. Regulated protein depletion by the auxin-inducible
905 degradation system in Drosophila melanogaster. *Fly (Austin)*. 10:35-46.

906   Verma, R., D. Mohl, and R.J. Deshaies. 2020. Harnessing the Power of Proteolysis for Targeted Protein
907   Inactivation. *Mol Cell*. 77:446-460.
908   Wagner, R.E., and M. Frye. 2021. Noncanonical functions of the serine-arginine-rich splicing factor (SR)
909   family of proteins in development and disease. *Bioessays*. 43:e2000242.
910   Wegener, M., and M. Müller-McNicoll. 2019. View from an mRNP: The Roles of SR Proteins in Assembly,
911   Maturation and Turnover. *Adv Exp Med Biol*. 1203:83-112.
912   Yamaguchi, N., T. Colak-Champollion, and H. Knaut. 2019. zGrad is a nanobody-based degron system that
913   inactivates proteins in zebrafish. *Elife*. 8.
914   Yu, H., and A. Matouschek. 2017. Recognition of Client Proteins by the Proteasome. *Annu Rev Biophys*.
915   46:149-173.
916   Zheng, N., B.A. Schulman, L. Song, J.J. Miller, P.D. Jeffrey, P. Wang, C. Chu, D.M. Koepp, S.J. Elledge, M.
917   Pagano, R.C. Conaway, J.W. Conaway, J.W. Harper, and N.P. Pavletich. 2002. Structure of the Cul1-Rbx1-
918   Skp1-F boxSkp2 SCF ubiquitin ligase complex. *Nature*. 416:703-709.
919   Zheng, X., Q. Peng, L. Wang, X. Zhang, L. Huang, J. Wang, and Z. Qin. 2020. Serine/arginine-rich splicing
920   factors: the bridge linking alternative splicing and cancer. *Int J Biol Sci*. 16:2442-2453.
921   Änkö, M.L. 2014. Regulation of gene expression programmes by serine-arginine rich splicing factors. *Semin*
922   *Cell Dev Biol*. 32:11-21.
923   Änkö, M.L., M. Müller-McNicoll, H. Brandl, T. Curk, C. Gorup, I. Henry, J. Ule, and K.M. Neugebauer. 2012.
924   The RNA-binding landscapes of two SR proteins reveal unique functions and binding to diverse RNA
925   classes. *Genome Biol*. 13:R17.
926